Headward growth and branching in subterranean channels

Arshad Kudrolli,* Nikolay Ionkin, and Andreea Panaitescu
Department of Physics, Clark University, Worcester, Massachusetts 01610, USA
(Received 13 July 2017; published 17 November 2017)

We investigate the erosive growth of channels in a thin subsurface sedimentary layer driven by hydrodynamic drag toward understanding subterranean networks and their relation to river networks charged by ground water. Building on a model based on experimental observations of fluid-driven evolution of bed porosity, we focus on the characteristics of the channel growth and their bifurcations in a horizontal rectangular domain subject to various fluid source and sink distributions. We find that the erosion front between low- and high-porosity regions becomes unstable, giving rise to branched channel networks, depending on the spatial fluctuations of the fluid flow near the front and the degree to which the flow is above the erodibility threshold of the medium. Focusing on the growth of a network starting from a single channel, and by identifying the channel heads and their branch points, we find that the number of branches increases sublinearly and is affected by the source distribution. The mean angles between branches are found to be systematically lower than river networks in humid climates and depend on the domain geometry.

DOI: 10.1103/PhysRevE.96.052904

I. INTRODUCTION

Channel networks which carry fluid through a heterogeneous medium and evolve as they erode, transport, and deposit sediments are common in nature [1–3]. For example, river networks formed due to the confluence of tributaries drawn from a wide basin as they follow the gradient of the land are an enduring feature across the face of the earth [3–5]. Though less obvious, channel networks can also develop in the subsurface in natural aquifers and in enhanced oil recovery [6–8]. While dissolution of the medium can play an important role in the development of subterranean channels and sinkholes [9–11], the internal erosion of sedimentary grains by the drag of the fluid flow can by itself lead to evolution of porosity in the subsurface [8,12–17]. Thus, the growth of channels due to erosive fluid flow through a sedimentary medium is a problem of wide-ranging interest.

A number of models have been developed to examine evolution of channel networks at the earth's surface coupling hill slope and fluid flow [18–20]. It has been shown that river channel branches in humid climate areas of the United States appear to meet distributed around an angle of 72° [21]. This angle corresponds to the stable angle in which headward growing channels can be expected to evolve in a domain in which the fluid flow is governed by the Laplace equation. More acute angles are observed in more arid climates [22]. It is noteworthy that the equation that governs the flow of the fluid in a two-dimensional (2D) porous medium is similar to that used to describe ground water flow in the Dupuit approximation [23]. While statistical comparison with venation patterns in leaves [24] among branching networks has been conducted [25], we are unaware of any detailed comparison with subsurface channels because of lack of appropriate data. Thus, the connection of channel networks observed on the earth's surface and those that develop due to internal erosion in the subsurface remains far from clear.

Recently, a model system was developed to investigate the growth of heterogeneity due to erosion when a fluid is forced across a granular bed [6]. The solubility and the cohesivity of the granular medium in these experiments are negligible by design. Channels were observed to form over time because of a feedback of increased fluid flow drawn to regions with higher porosity resulting from bed erosion. It was further shown that the fluid flow through the medium can be modeled using Darcy's law. Hence, the equation which describes the flow through the heterogeneous medium is given by

$$\nabla \cdot (\kappa \nabla P) = 0, \tag{1}$$

where P is the local pore pressure, and κ is the local permeability, which varies spatially and temporally as the bed evolves. This equation can be solved for given boundary conditions, which in this case correspond to constant pressure in the inlet and outlet reservoirs, and a prescribed flow rate through the system. Then the mean fluid flow is given by

$$\mathbf{v}_f = -\kappa \nabla P. \tag{2}$$

The calculated fluid flow was shown to be consistent with experimental observations, and the interface between the regions with low and high porosity was observed to erode, on average, when the local fluid velocity exceeded a critical value J_c corresponding to the erodibility of the medium.

Building on these observations, a hybrid erosion model was also developed [6] in which the porous medium was divided into three components consisting of the immobile granular phase corresponding to the porous solid phase, mobile granular phase, and fluid phase following Ref. [26]. By solving Eq. (1) for a given spatial porosity distribution and boundary conditions, and then calculating the fluid flow using Eq. (2), the hydrodynamic stress acting on the medium is found throughout the system. We test for regions which are above the threshold of erosion of the medium drawn from a random distribution with the same mean and standard deviations as observed with single grain motion. Then the immobile solid phase in these regions is converted to the mobile granular phase provided they exceed the critical value and are not locked in because of the presence of other grains which impede their motion.

*akudrolli@clarku.edu

The dislodged granular phase is moved along with the fluid for a given time interval, but with a fraction of the speed because of frictional losses. The granular phase is assumed to be deposited if the local fluid flow falls below a critical value, or if the path of the grain is blocked by the presence of other grains. Using this model, it was demonstrated that erosion develops at interfaces between regions with low and high porosity, with channels developing in regions with concave interfaces, which increasingly focus fluid flow. Thus, erosion can occur at average flux J through the medium at significantly lower flux compared to the mean flux required to erode a single grain J_c depending on the interface curvature [6].

In this paper, we build on those results by focusing on the growth of channels and their bifurcations in response to fluid flow under various imposed boundary conditions. In order to further simplify the analysis, we modify the system so that grains exit only at a narrow outlet. A similar geometry has been used to examine channel growth driven by ground water flow at the bed surface to understand the growth of their transect [27], and contribution of local rainfall on the shape of channel growth versus far field groundwater sources [23]. Further, we examine two conditions near the outlet: one in which the fluid is also forced to exit through the narrow outlet giving rise to convergent fluid flow, and the other where the fluid is not imposed to converge through the outlet. In the latter case, convergence of the fluid flow occurs as a channel grows and thus can be thought to occur naturally. We show that the interface between high- and low-porosity regions becomes unstable with channels growing depending on the imposed flux. Both coarsening and bifurcation dynamics is observed as the branched channel network grows. Focusing on the growth of a network starting from a single channel, we examine the number distribution of branches and the angle between branches, and compare and contrast them with branched river networks.

II. MODEL SYSTEM

Figure 1(a) shows a schematic diagram of the experimental system in which water is driven through a porous medium inside a thin horizontal Hele-Shaw cell and is modified from the one used previously to study curvature-driven growth of channels in an erodible porous medium [6]. As in that work, we use a quasi-2D geometry to simplify the experimental system to enable us to identify the regions which erode, and where grains deposit as the porosity evolves. Further, it allows us to link more quantitatively the experimental parameters with those that have to used in the complementary simulations to understand the progress of erosion and channels. The length L of the system is 28.5 cm, and the width W is 28.5 cm. The porous medium consists of glass beads with diameter $d = 1.21 \pm 0.1$ mm with density 2500 kg m^3. The fluid is injected into the inlet reservoir with a prescribed flow rate Q using a peristaltic pump. Then it is allowed to enter the medium either all across the top boundary or near the corners by placing a physical barrier across most of the top boundary as shown in the schematic diagram. These two fluid source conditions are called uniform and nonuniform injection, respectively, in the following discussion. In either case, the grains are allowed to leave the cell only through a $W_o = 2.5$ cm wide gap at the center of the bottom side wall. By allowing the grains to exit the cell, we focus on the dynamics of channel growth from a point which serves as an ideal sink, beyond which sediment transport can be considered to be unimportant to the development of the channels upstream.

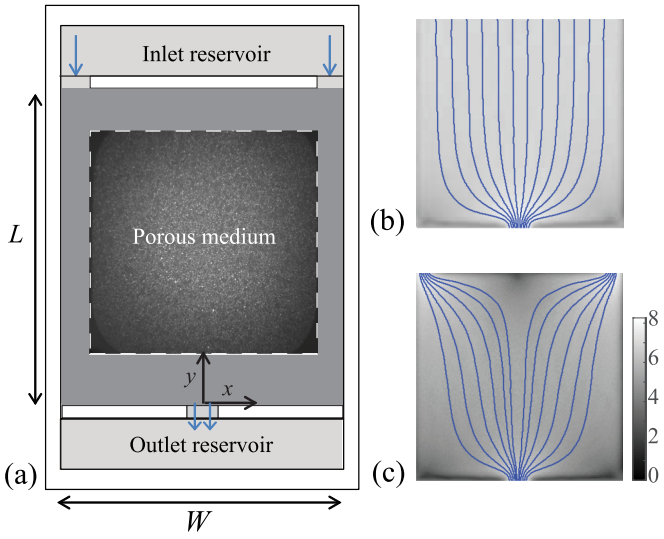

FIG. 1. (a) Schematic of the experimental system. Fluid enters the porous granular bed through the top boundary from a reservoir either all across or near the two corners. An image of the initial medium corresponding to the area that can be visualized in the experiments is also shown. The fluid is injected into the inlet reservoir with a prescribed flow rate and is allowed to exit from an outlet at the center into a reservoir which can also collect the eroded material. (b, c) The calculated magnitude of the fluid velocity for the prescribed boundary conditions along with streamlines (black and blue lines). The gray scale bar and the numbers corresponds to the velocity V scaled by the injection flux J.

The medium is prepared by slowly pouring and spreading the grains evenly in a monolayer on a horizontal optically smooth glass plate and then covering the bed with a parallel transparent glass plate to allow imaging. The system is then sealed to prevent leaks. The top and bottom surfaces of the resulting Hele-Shaw cell are separated by distance $h = 1.5d$, allowing the grains to move freely when they are dislodged. We find this to be an optimal separation distance based on preliminary experiments. If a larger distance is used, then the grains have a tendency to stack in two layers in a hexagonal close-packed structure, which makes it difficult to track the local volume fraction besides making them difficult to dislodge. If a smaller distance closer to d is used, some of the larger grains in the sample can get stuck between the plates, overall increasing the threshold to dislodge grains and decreasing their mobility.

To characterize the amount of disorder in the initial bed packing, we measure the local packing fraction of the prepared bed. An image is taken of the bed where individual grain positions can be identified to within a tenth of the grain diameter. As seen from Fig. 2(a), the packing fraction of the grains ϕ_g defined as the volume of the grains in a Voronoi cell is observed to be distributed around a mean volume fraction $\phi_m = 0.41$, where the Voronoi cell volume corresponds to the

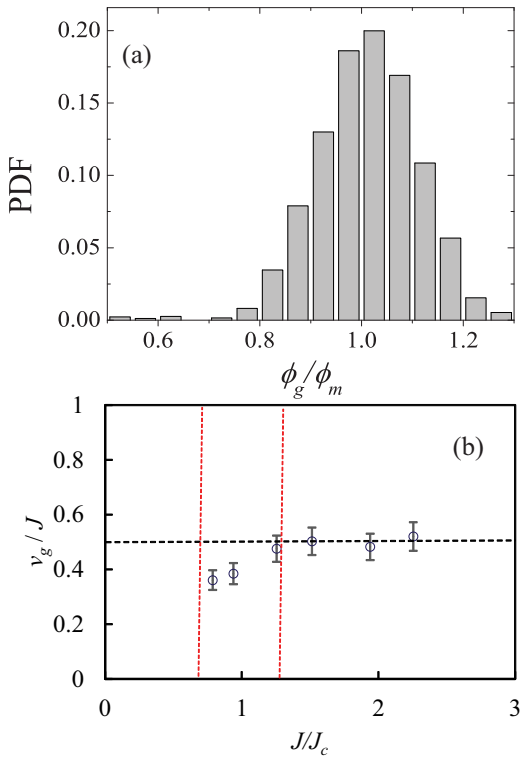

FIG. 2. (a) The distribution of the local granular packing fraction ϕ_g measured using the Voronoi cell size. The mean volume fraction $\phi_m = 0.41$. (b) The ratio of the mean grain speed v_g and the prescribed mean fluid flux J as a function of J/J_c. The vertical dashed lines indicate range of critical flow required to erode a grain at rest on the substrate. The error bars indicate the percentage range of measured v_g from grain to grain.

area in the horizontal plane which is closest to a grain center compared to its nearest neighbors times the separation between top and bottom surfaces of the experimental cell. This observed distribution of values corresponds to ϕ_g between 0.37 and 0.45 is somewhat greater than in previous experiments [6]. The differences arise because of the slight variation in the preparation technique. In that study the initial grains were rolled down a slightly inclined substrate to more uniformly fill the experimental cell. That exact protocol is not possible with the current boundary conditions used here and thus results in slightly higher fluctuations. The permeability of the medium κ depends on the volume fraction of the grains ϕ_g, and is given by the function $\kappa = 0.285\,(1 - 2.14\phi_g)$ mm^{-2} [6]. We find it convenient to define a fluid flux $J = Q/Wt$, which is easier to compare across systems with different dimensions rather than the flow rate Q.

By performing further experiments with a few isolated grains in the same cell, but with uniform inlet and outlet so that the fluid flow is uniform across the cell, we find that the average fluid flux required to dislodge a particle is $J_c = 26.3$ mm s^{-1} due to the friction with the substrate. Further, because of the size distribution of the grains and their roughness, the grains are observed to dislodge over a wide range of flux which is of order $\pm J_c/3$. The Reynolds number Re of the fluid flow at the grain scale is given by $\mathrm{Re} = Ud/\eta$, where U is the fluid speed, and $\eta = 0.89$ mm^{2}s^{-1} is the kinematic viscosity for water at 25 °C. Then we have $\mathrm{Re} \approx 40$ for $U \approx J_c$. At these Re, the drag has both viscous as well as inertial contributions [28]. The grains dislodge when the torque due to the hydrodynamic drag increases above the torque due to gravity about a pivot point given by the roughness of the grains [28,29].

Once dislodged, the grains are observed to move rapidly along with the fluid flow speed. To quantify the speed relative to the fluid flux, we measure the speed of the grains v_g as a function of imposed average fluid flux J by placing individual grains in an otherwise empty cell with a rectangular cross section for which the fluid flow profile is known [30]. A sequence of images was recorded with a frame rate of 1 per second while the grain were in motion, and the speed obtained by measuring the distance moved between frames. The grains were observed to move with a constant speed very soon after being dislodged.

Figure 2(b) shows the measured speed of the grains as a function of the prescribed flux. The grain speed v_g is observed to be approximately half the critical flow speed fluid flow speed required to dislodge the grain. While the recorded speed was observed to fluctuate from grain to grain as shown by the error bars, the speed of a grain was more or less constant as it moved across the cell. Further, no systematic difference was noted if the particle moved down the center of the cell or near the sides of the cell. This is consistent with the fact that the fluid flow is essentially uniform in a thin Hele-Shaw cell. From this observation, we conclude that the grain speed can be assumed to be approximately 50% of the fluid flux, once dislodged, irrespective of the location within a channel.

We numerically solve Eq. (1) using the method of relaxation after discretizing the system in a square grid corresponding to a $2d \times 2d$ area to obtain the coarse-grained fluid flow through the porous medium. The local magnitude of the local fluid velocity $V = |\mathbf{v}_f|$ is then obtained using Eq. (2). The magnitude of the fluid velocity and the streamlines are plotted in Fig. 1(b) in the case of uniform injection, and in Fig. 1(c) in the nonuniform injection case in otherwise identically prepared beds with $\phi_g = 0.41 \pm 0.04$. One can observe that the flow in the top half near the inlets are quite different, while the flow near the outlet is similar.

To quantitatively compare the velocity profiles, we plot the magnitude of the fluid velocity V across the width of the cell corresponding to $y = 0.67L$ in Fig. 3(a), and at a fixed distance $0.1L$ as a function of the angle θ from the x axis in Fig. 3(b) for the uniform injection case. Similarly, we plot V for the nonuniform injection case corresponding to $y = 0.67L$ in Fig. 3(c), and at a fixed distance $r = 0.1L$ in Fig. 3(d). We observe that the profiles are different at the top, but look identical down to the fluctuations near the outlet in Figs. 3(b) and 3(d). Thus, the effect of the details of the injection profile is unimportant by the time the fluid reaches the area near the outlet, and the spatial variations in the fluid velocity there are dominated by the local medium fluctuations.

Further, to understand the effect of volume fraction fluctuations on the measured fluid velocities, we performed simulations with $\phi_g = 0.41$, where fluctuations are absent, i.e., $\Delta\phi_g = 0$. We plot V as a function of width corresponding to $y = 0.67L$ in Fig. 3(e), and at a fixed distance $r = 0.1L$ from the center of the exit in Fig. 3(f). We observe that while V has several shallow peaks in the case of $\Delta\phi_g = \pm 0.04$

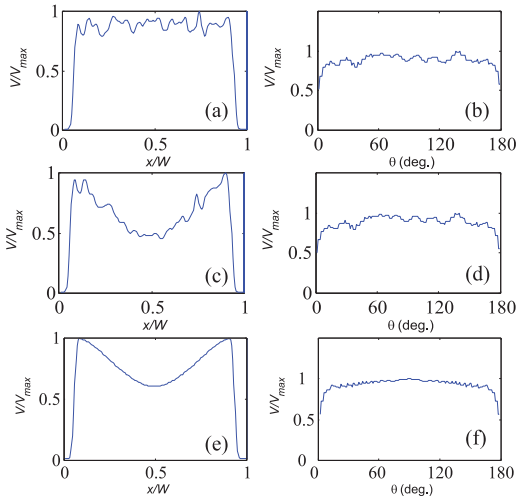

FIG. 3. (a) The fluid velocity V obtained using numerical simulations normalized by the maximum velocity $V_{\max}$ at $y = 0.67L$ (uniform injection, $\Delta\phi = \pm 0.04$). (b) $V/V_{\max}$ at distance $r = 0.1L$ from outlet (uniform injection, $\Delta\phi = \pm 0.04$). (c) $V/V_{\max}$ at $y = 0.67L$ (nonuniform injection, $\Delta\phi = \pm 0.04$). (d) $V/V_{\max}$ at $r = 0.1L$ from outlet (nonuniform, $\Delta\phi = \pm 0.04$). (e) $V/V_{\max}$ at $y = 0.67L$ (nonuniform, $\Delta\phi = 0.0$). (f) $V/V_{\max}$ at $r = 0.1L$ from outlet (nonuniform, $\Delta\phi = 0.0$). Velocity $V/V_{\max}$ is observed to be large along multiple directions when ϕ_g fluctuates, but the velocity is peaked along the symmetry axis when fluctuations are absent.

shown in Figs. 3(b) and 3(d), a single broad peak occurs corresponding to $\Delta\phi_g = 0$ shown in Fig. 3(f). Thus, the presence of fluctuations leads to symmetry breaking and several possible directions for initial erosion of channels. As we shall see, the velocity profiles and the fluctuations can be used to understand the spatial distribution of the channels.

III. GROWTH OF CHANNELS

A. Experiments

We now discuss the erosion observed in the experiments performed with the two different injection geometries shown in Figs. 1(b) and 1(c). The flux through the system was increased with a ramp rate $\alpha_J = 0.1$ mm s^{-2}, and the bed was imaged as a function of time. Because of the convergent nature of the flow near the outlet, the mean fluid speed decreases approximately inversely as the distance to the outlet for distances up to $W/2$. Thus, the flux through the system has to be ramped up to continue erosion even after the channel is initiated as the channel moves into regions which have lower velocity. We coarse-grain the images in $2d \times 2d$ area to obtain the average volume fraction of the grains ϕ_g and then plot the contour corresponding to $\phi = 0.35$ which separates regions with high- and low-volume fraction of grains in Figs. 4(a) and 4(b). We observe in both cases that channels form near the outlet which appear to initially radiate out in multiple directions. Unlike previous work where deltas form near the mouth of the channels [6], the eroded grains are observed to be carried out of the system as the fluid moves more rapidly as it converges to the outlet. Over time, channels develop headward

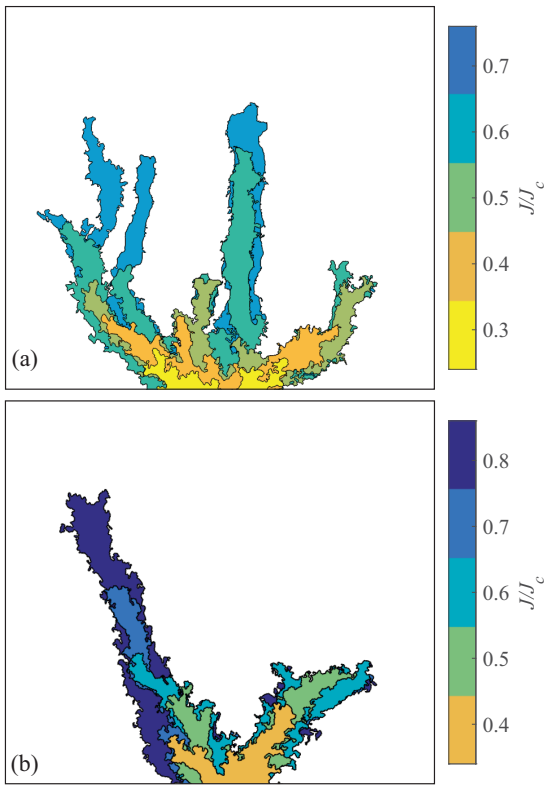

FIG. 4. A contour map of the front between volume fraction region corresponding to $\phi_g = 0.35$ observed in the experiments as the flux J/J_c is increased in (a) the uniform injection case and (b) the nonuniform injection case. The channels develop at a lower value of J compared with J_c because of the convergence of the flow near the outlet. Several channels develop near the outlet, but only a few advance upstream toward the inlet. The bounding box corresponds to the viewing area shown in Fig. 1(a).

toward the fluid source as the bed continues to eroded because of the action of the fluid.

In comparing the two examples, we observe that the initial development of channel appears similar but over time, channels grow more toward the corners in the nonuniform injection case where the fluid is injected in the corners. Furthermore, one observes that the growth of the channel toward one of the corners grows faster due to spontaneous symmetry breaking that leads to more fluid being drawn to it resulting in still faster growth. Thus, the boundary conditions and the resulting distribution of the fluid flow inside the medium play a significant role in the development of the channels in the experiments.

B. Simulations

To understand the spatial growth of the channels in relation to the fluid flow and the disorder, we performed a set of simulations with the erosion model using the size and boundary conditions used in the experiments. Figures 5(a)–5(d) and Figs. 5(e)–5(h) show the result of example simulations corresponding to uniform injection and nonuniform injection, respectively. As in the experiments, one notes that the channels appear to radiate out from the outlet initially before curving

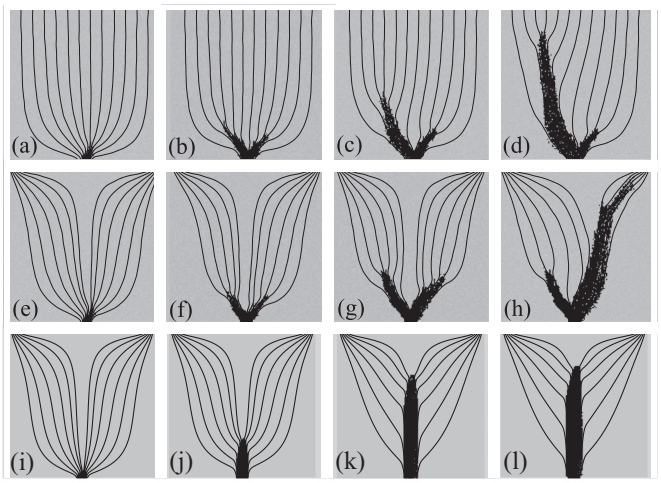

FIG. 5. (a–d) Evolution of channels observed in the simulations for the uniform injection case. (a) $t_s = 250$, $J/J_c = 0.13$, (b) $t_s = 350$, $J/J_c = 0.18$, (c) $t_s = 600$, $J/J_c = 0.29$, and (d) $t_s = 800$, $J/J_c = 0.37$. (e–h) Evolution of channels observed in the simulations for the nonuniform injection case. The ramp rate $\alpha_J = 0.1$ mm s^{-2}. (e) $t_s = 250$, $J/J_c = 0.13$, (f) $t_s = 500$, $J/J_c = 0.24$, (g) $t_s = 800$, $J/J_c = 0.38$, and (h) $t_s = 900$, $J/J_c = 0.42$. (i–l) Evolution of channels observed in the simulations for the nonuniform injection case with $\Delta\phi = 0$. The ramp rate $\alpha_J = 0.1$ mm s^{-2}. (i) $t_s = 250$, $J/J_c = 0.13$, (j) $t_s = 500$, $J/J_c = 0.24$, (k) $t_s = 800$, $J/J_c = 0.38$, and (l) $t_s = 900$, $J/J_c = 0.42$. The channel is not observed to bifurcate under the same driving conditions when the volume fraction is uniform.

toward the boundary with the inlets. The reason for this trajectory of the channel head becomes clear by examining the streamlines, which are also plotted in Fig. 5. The streamlines are observed to converge symmetrically initially near the outlet of erosion, but then get increasingly focused to the channel head as it grows further into the bed.

While more than one channel starts to grow initially, we find a single channel eventually spans across the porous medium, as in the experiments shown in Fig. 4. As is clear from the streamlines, this occurs because the channel which grows further draws more water away from the smaller channels, leading them to eventually stop growing as the fluid flow to those channels falls below the threshold for erosion. Further sets of simulations were performed corresponding to the applied conditions but using different random initializations of the spatial volume fraction distribution of the porous medium and the threshold for the erosion of the medium. We find that the initial number of channels and the order in which they grow can fluctuate from run to run as in the experiments. Irrespective of these details, it was observed that a single channel would eventually dominate and grow toward one of the inlets for this system size.

Comparing and contrasting the development of the channels under the two boundary conditions shown in Fig. 5, one observes that channels appear to grow more toward the middle of the bed in the uniform injection case, whereas the channels grow toward one of the corners in the nonuniform injection case. Further, two channels grow initially in the examples shown, but only one of the channels dominates as it draws increasingly more fluid as it grows.

In the case of the growth of channels with nonuniform injection, one also observes that the channel which eventually spans the system in fact was initiated at a later time before eventually growing faster and drawing more fluid compared to the other incipient channels. Similar randomness in the order of the evolution can be noted in the experimental data as well. While a channel grows initially faster in one direction in Fig. 4(b) up to $J/J_c = 0.5$, a second smaller channel that develops later grows faster and eventually spans the system as it grows toward the fluid source. Thus, grain-scale disorder also plays a significant role in the eventual evolution of the channels in addition to the coarse-grained spatial distribution of the fluid velocity obtained from Eq. (2).

We also performed simulations by assuming that ϕ_g was the same throughout the domain, i.e., $\phi_g = 0.41$, but otherwise similar driving parameters. As shown in Figs. 5(i)–5(l), a single channel was observed to develop across the symmetry axis in this case even when the flow is injected in the corners. This occurs because V has a maxima along the axis of symmetry as shown in Fig. 3(d). Because there is no variation in the erodibility properties of the medium, the area near the outlet starts to erode symmetrically. As this draws more water along the axis of symmetry, a channel still develops as opposed to a uniformly expanding amphitheatre shape, even in this homogeneous volume fraction case. Since the eroded channel is symmetric, the resulting flow is symmetric, and the channel is not observed to bifurcate and continues to erode along the axis of symmetry of the domain. Thus, the presence of fluctuations in the porosity of the medium is crucial to the overall spatial development of the channels.

C. Evolution of channel length

In order to quantify the growth of the channels, and the phenomena discussed above, we identify channels using methods discussed in the Appendix. We then obtain the length of the longest channel l_e, and plot it as a function of imposed flux J normalized by the mean flux J_c for uniform and for nonuniform injection in Fig. 6(a). Because we cannot visualize the medium close to the boundaries as shown in Fig. 1(a), the lengths of the channels are shown only when they enter the viewing area and up until they leave the viewing area toward the inlet. Thus, it should be noted that the channels start to grow at a lower J/J_c than is apparent from Fig. 6(a). This value can be estimated from the fact that all the fluid injected into the system is forced out through the narrow outlet with width W_o. Thus the fluid flow near the outlet is a factor W/W_o higher than the mean flux J across the entire width of the system.

In both cases, we observe that the length of the channel shows stick-slip motion. We performed additional sets of experiments corresponding to each boundary condition. While the features discussed above were observed in each of these experiments, considerable differences were also observed in the onset of erosion and the detailed development of channels that we attribute to variation in the preparation of the bed, i.e., the higher overall flux required to erode a channel of a given

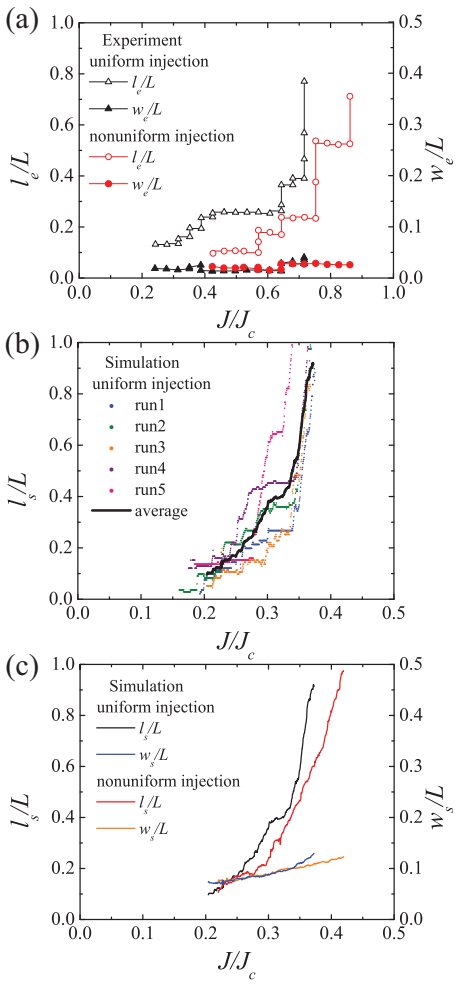

FIG. 6. The length l_e and the width w_e of the main channel in the experiments shown in Fig. 4 as a function of flux J/J_c in the case of uniform and nonuniform injection. (b) The length l_s of the main channel in the five different simulations each shows stick-slip motion as in the experiments, but increases faster than in the experiments (see text). (c) The length and width of the channels averaged over the five simulations for uniform and nonuniform injection cases grow similarly, although somewhat systematically faster in the uniform injection case as the length grows.

length in the nonuniform injection case is within the variation observed in the case of each boundary condition.

To quantify the width of the channels, we plot the average width of the main channel observed in the experiments w_e and in the simulations w_s in Figs. 6(a) and 6(c). We observe the widths grow significantly more slowly than the length, and the channels become essentially one-dimensional objects as the channels reach the domain size.

We also plot the length l_s of the longest channel for the two cases as a function of J/J_c in Fig. 6(b) for five example simulations prepared with different spatial initialization of the porous medium and erodibility thresholds but with nonetheless the same mean values. It can be observed that the channel length in the simulations also displays stick-slip motion in each run, but with somewhat small step sizes than in the experiments. Furthermore, the channel length increases

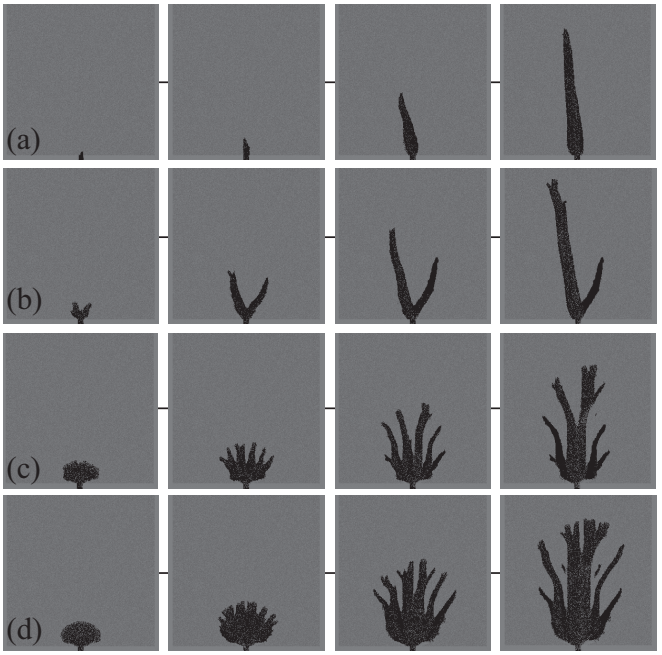

FIG. 7. Evolution of erosion patterns starting from various fluid flux J_o. (a) $J_o/J_c = 0$; $t = 640$ s, 1600 s, 3200 s, and 4000 s. (b) $J_o/J_c = 0.22$; $t = 320$ s, 500 s, 1440 s, and 1920 s. (c) $J_o/J_c = 0.44$; $t = 320$ s, 480 s, 800 s, and 1120 s. (d) $J_o/J_c = 0.66$; $t = 320$ s, 380 s, 800 s, and 1120 s. Higher initial flux gives rise to more branched patterns.

more rapidly with J/J_c in the simulations compared to the experiments. These differences appear to be due to the inherent nature of the simulations where the permeability is coarsened over the scale of a few grain diameters, and thus the calculated fluid velocities have fewer fluctuations compared to the experimental system. Additional important factors are that the erosion model is local and does not take into account frictional aging and collective jamming effects present in the experimental system. Even with these simplifications, the simulations capture the overall effect of the boundary conditions on the spatial and temporal evolution of the erosion channels.

D. Erosion front instability

We next examine conditions which give rise to a single channel versus branched-channel growth. Focusing on the uniform injection case, a set of simulations were performed where the total prescribed flow rate was increased starting at initial flux J_o as shown in Fig. 7. In these simulations, the bed was initialized identically in terms of the spatial distribution of the volume fraction and erodibility to isolate the effect of the imposed flux on the channel network evolution. Further, the simulation size was increased to a 300×300 grid to obtain a more detailed evolution of the patterns. Figure 7 shows examples as the flux is increased linearly starting from J_o, i.e., $J = J_o + \alpha_r t$, with $\alpha_r = 0.1$ cm s^{-2}. When the flux is increased from zero, one observes that a single channel develops and then grows across the domain toward the fluid source. As J_o is increased, one observes from Fig. 7 that the erosion front separating regions with high and lower porosity

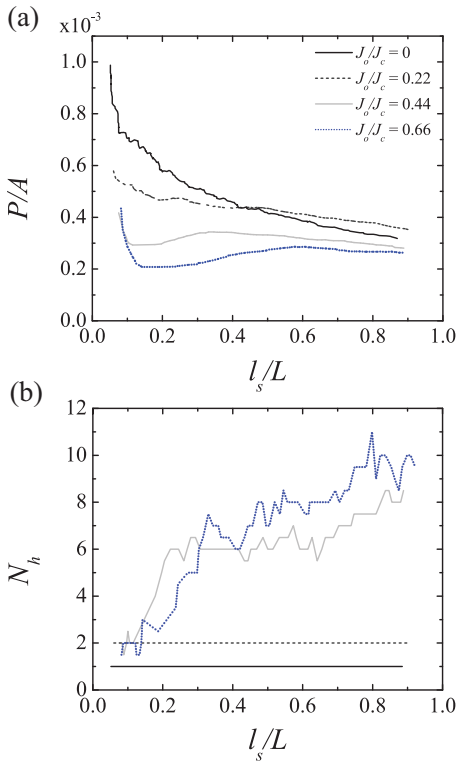

FIG. 8. (a) The perimeter of the region where erosion has occurred and $\phi_g < 0.25$ compared to its area ($L = 28.5$ cm). The ratio is observed to decrease corresponding to growth of linear structures, i.e., channels. (b) The total number of channel heads as a function of length of the longest channel is observed to grow with increasing J_o/J_c. The rate of growth of number of channels is observed to decrease as the channel length grows.

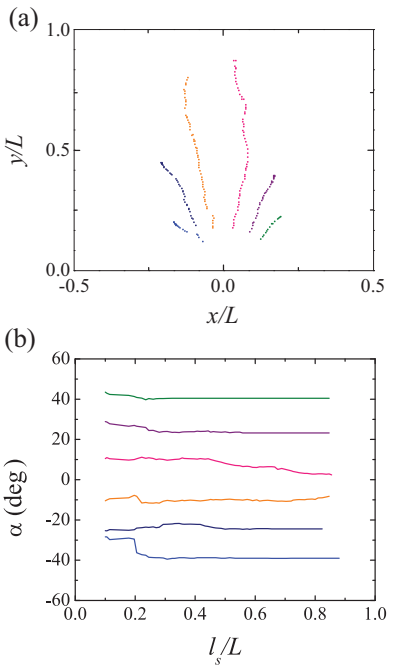

FIG. 9. (a) The positions of the main channel heads over time corresponding to $J_o/J_c = 0.44$ shown in Fig. 7(c) plotted in time increments of 12 seconds ($L = 28.5$ cm). The tracks show that the channels grow radially outward initially. The ones closer to the water source are observed to grow further and bend toward the water source. (b) The evolution of the corresponding angle α between the direction that the channels grow and the y axis as a function of the length l_s of the longest channel.

expands out uniformly at first, before becoming unstable with an increasing number of fingers developing over time.

To quantify these trends, we identify the properties of the eroded regions using the volume fraction maps as discussed in the Appendix. To check that bifurcated network is indeed channel-like, we extract the perimeter of the eroded region P and the its area A as a function of time. We then plot the ratio P/A as a function of the length of the longest channel l_s in Fig. 8(a). In the case of the lowest J_o/J_c, we observe that the ratio smoothly decreases as the erosion progresses, and the eroded region becomes increasingly longer compared to wider, leading to a channel-like object. As J_o/J_c is increased, where the pattern looks increasingly bifurcated, we observe that the ratio also decreases overall and starts approaching similar values as in the case of a single channel.

Figure 8(b) shows N_h plotted as a function of l_s/L for each of the cases shown in Fig. 7. In the case of $J_o/J_c = 0$, we identify a single channel as it grows across the system. As J_o/J_c is increased, two channel heads are observed to form consistent with the bifurcated pattern observed in Fig. 7(b). The number of channel heads are observed to increase rapidly as J_o/J_c is increased further and channels start to bifurcate. One can understand the development of the increasing amount of branching with flux by examining the variation of the fluid velocity V with angle θ in Fig. 3(b). Because of the spatial variation of ϕ_g, V has multiple local maxima as a function of θ. Nonetheless, a unique maximum does exist corresponding to $V_{\max}$ along which one can expect the fluid to erode the medium when the imposed total flux is increased slowly to always be near the threshold of erosion. However, if the flux is stepped up rapidly, the medium is above the erosion threshold to an increasing distance from the outlet. This leads to a uniformly expanding erosion front at early times. However, as the front advances upstream, V on average decreases inversely as the distance to the outlet because of the convergent nature of the flow near the outlet. Thus, one expects the erosion to become increasingly sensitive to the local variation of V as the front advances. Any perturbation of the front can then lead to regions with varying concavity. Because regions with higher concavity draw relatively more fluid as shown previously [6], such regions erode faster at the expense of neighboring regions leading to the formation of a channel. The initial uniform front expands outward to a larger distance with J_o before giving rise to an increasing number of sites along the front which encounter fluctuations in the medium. Thus, the number of channels grows with J_o as can be noted from Fig. 8(b).

This can be quantitatively noted from the positions of the channel head of the main channels that develop when $J_0/J_c = 0.44$ as shown in Fig. 9(a). The main channels are first identified here when the length becomes at least as long as their width, and show that they form after the eroded region expands out somewhat uniformly in all directions from the outlet. One observes that the channels then radiate outward as they grow upstream, with the channels closer to the source growing faster.

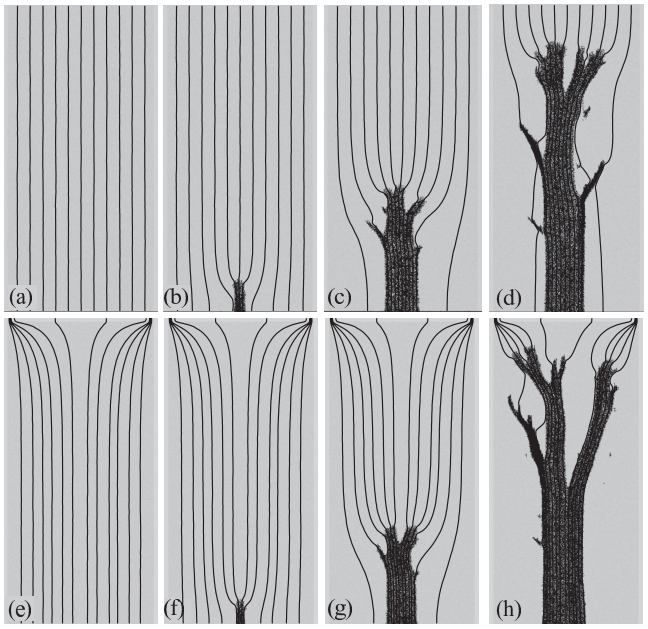

FIG. 10. Evolution of a branched channel when grains are only allowed to leave near the center of the bottom side boundary but fluid is allowed to flow out everywhere along the bottom boundary in the case of uniform injection (a–d) and nonuniform injection (e–h). The imposed flow corresponds to (a) $J/J_c = 0.45$, (b) $J/J_c = 0.55$, (c) $J/J_c = 0.61$, and (d) $J/J_c = 0.69$. (h) (a) $J/J_c = 0.45$, (b) $J/J_c = 0.57$, (c) $J/J_c = 0.69$, and $J/J_c = 0.72$.

Further, a subtle turning of the channels can also be noted as they grow. To quantify this, we plot the angle α between the orientation of the channels and the y axis in Fig. 9(b). One can note that in each case α decreases toward zero as they grow, the only exception being the channel on the side, which stops growing after a while. As these central channels evolve, they appear to further exhibit bifurcations as they grow in length, while the growth of the channels on the sides appears to cease at later times. Thus, a complex interaction of fluid flow and porosity is observed to develop over time giving rise to a rich set of bifurcating channels depending on the initial driving flux.

IV. DEVELOPMENT OF FLUID CONVERGENCE AND BIFURCATIONS

We now examine how channels grow and bifurcate starting from conditions where convergent flow is not imposed initially as in the experiments and simulations discussed in the previous sections. We implement this in our system by allowing the fluid to leave the domain everywhere across the bottom boundary, and not just through the central outlet where grains are allowed to erode. Examples of the initial flow before erosion occurs are shown in Figs. 10(a) and 10(e) for uniform and nonuniform injection, respectively. Under these conditions, a single channel can grow upstream initially, enabling us to examine its growth and bifurcation without the complexity of channel-channel interactions near the outlet.

Simulations were performed corresponding to $L/W = 2$, besides with $L/W = 1$ as in the simulations discussed in the previous sections, to examine the development of the channel network over a larger domain. Figure 10 shows snapshots corresponding to branched channel networks which develop in simulations corresponding to $L/W = 2$ for both uniform and nonuniform injection cases. Here the imposed flux is ramped up with $\alpha_J = 0.1$ mm s^{-1}, the same as in the previous simulations. The eroded regions are denoted in black, and the fluid streamlines are indicated by solid lines. We find that a single channel forms initially, leading to a convergent flow near its head as the fluid is diverted to regions with higher porosity. Thus, by contrasting the initial development here versus those discussed in the previous sections, one can readily note the initial spatial development of channels clearly carries the impact of the presence or absence of convergent flow near the outlet.

Further examining Fig. 10, one notes that branches grow over time in both cases as the channel advances. For distances sufficiently far away from the inlet, the differences in the source distribution does not affect the spatial distribution of the fluid flow. However, it is clear that channels appear to branch somewhat more broadly in the nonuniform injection case as the branched network continues to evolve toward regions where the fluid enters the domain. One can also observe that the side branches, which form at earlier times, stop evolving significantly as the fluid is drawn away by the advancing branches nearer to the source. These channels can be also closed-off by sediment that accumulate near their mouths, giving rise to isolated voids.

A. Growth rates

To quantitatively analyze the observed branched channel networks, we identify the branching points and channel heads with image processing methods discussed in the Appendix. We plot the length of the longest channel l_s observed as a function of the flux J in Fig. 11(a) for uniform injection. Five examples are plotted corresponding to different medium preparation but otherwise identical driving conditions. We observe that the length of the channels increases starting at different imposed flow rates. This occurs because of the different randomization of the initial local volume fraction distribution and erodibility in the medium even though the overall distributions and driving are identical. Nonetheless, once initiated, l_s appears to increase roughly similarly in each case.

It can be also noted the J/J_c at which channels form are also overall higher than in the cases discussed in the previous section for which l_s versus J/J_c is shown in Fig. 6(b). This is because the flow near the outlet is not convergent before channels form as opposed to the case in Fig. 4, where the fluid flow is forced to leave only through the outlet. This means that the mean flow at the outlet is higher in those cases by a factor given by the ratio of the width of the domain W and the width of the outlet compared with flow in the simulations discussed here, where the flow leaves more or less uniformly all along the bottom boundary as shown in Figs. 10(a) and 10(e).

To compare across the various simulations for the same driving conditions, we plot in Fig. 11(b) the mean length of the channel $\langle l_s \rangle$ as a function of time t from when the channels are first initiated t_o along with the error bar corresponding to

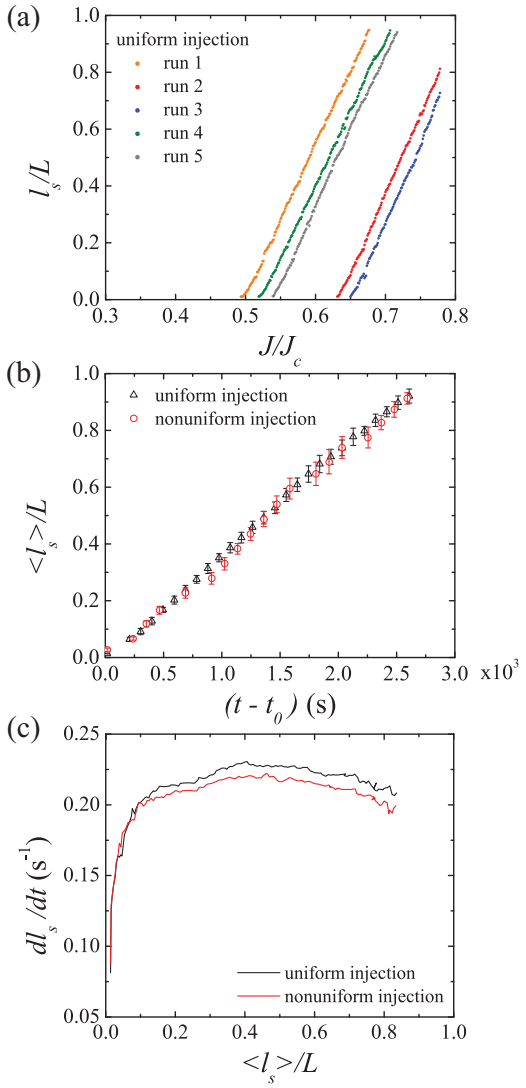

FIG. 11. (a) The length of the channels l_s/L as a function of imposed flow rate J/J_c for the five example simulations. The lengths increase steadily above a critical J/J_c with small variations from run to run with the different medium initializations. (b) The averaged $\langle l_s/L \rangle$ over the five runs plotted after a time when the channel is initiated is observed to nearly overlap for uniform and nonuniform injection. (c) The channel length growth rate is observed to increase initially and then remain more or less constant as the channel length increases before decreasing somewhat.

the mean square deviations. Thus, we find that the growth of the main channel is remarkably consistent from run to run.

We plot the mean rate of growth of the channel length dl_s/dt averaged over the five simulations as a function of the channel length l_s in Fig. 11(c) to examine the growth of the channels across the two conditions more closely. We observe that the rate increases at first before being essentially constant as the channel grows longer. The initial increase occurs because of the development of flow convergence as the channel first forms at the outlet. Plotting l_s and dl_s/dt in the nonuniform injection case in Figs. 11(b) and 11(c), respectively, one can note the overall growth over most of the length of the domain is similar. The nonuniform case is, however, somewhat lower

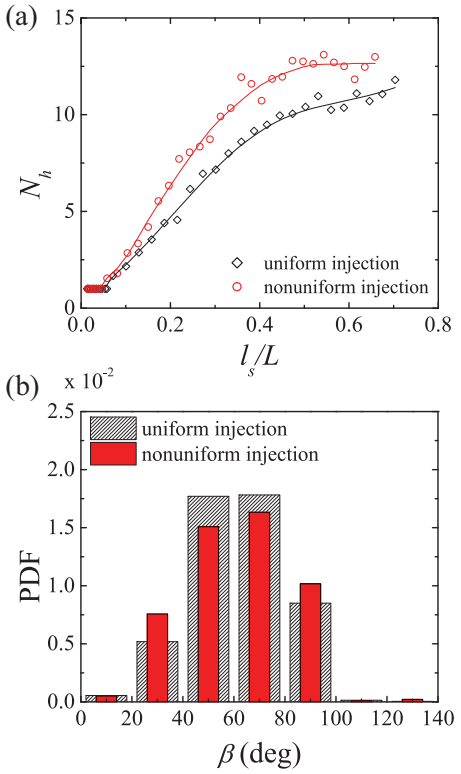

FIG. 12. (a) The number of channel heads N_h as a function of length of the longest channel l_s in the case of uniform and nonuniform injection. (b) Probability distribution function (PDF) of the angle between branches β in the case of uniform and nonuniform injection.

as the channels grow and bifurcate, and the source distribution becomes important.

B. Branching statistics

To characterize the observed channel bifurcations, we next examine the number of channel heads N_h as a function of l_s in Fig. 12 in the case of uniform and nonuniform injection. We note that N_h initially equals one before the channel bifurcates. Then N_h is observed to grow somewhat sublinearly with l_s as the channel branches and spreads wider before appearing to saturate. Now, exponential growth of branches may be expected if the rate of channel bifurcations is proportional to the number of channels present at a given time as appears to be the case in river branching distributions [31]. In those river networks, fluid can enter the system not only at the boundaries, but also throughout the domain via rainfall. Thus, screening plays an important role in our system with the number of branches stopping to grow, as older branches are coarsened out nearly at the same rate as the development of new branches.

Comparing the uniform and nonuniform injection cases, one observes that the initial bifurcations progress similarly because the influence of the fluid inlet distribution is negligible near the outlet. However, as l_s increases, one observes that N_h grows in the nonuniform injection case at a higher rate and saturates at a higher value compared to the uniform injection case. This is consistent with the example of the branched channel network for the two cases shown in Fig. 5,

where the branches in the nonuniform injection case appear more widely spread due to the fluid being injected at the corners.

We further characterize the branching observed in the network by measuring the angle β between neighboring branches. The distribution of angles observed in the five sets of simulations for the uniform and nonuniform injection cases is shown in Fig. 12(b). We observe that the distributions are similar but with slightly different mean angles $\beta_m = 61.3^\circ \pm 18^\circ$ and $\beta_m = 61.4^\circ \pm 20^\circ$ in the uniform and nonuniform injection case, respectively, for $L/W = 2$. Further, $\beta_m = 64.5^\circ \pm 17^\circ$ and $\beta_m = 65.2^\circ \pm 17^\circ$ in the uniform and nonuniform injection case, respectively, for $L/W = 1$. The distribution and the average value β_m is not found to depend significantly on the length of the channel beyond the bifurcation used to calculate the angles. The changes were found to be less than a degree if one uses points corresponding to 25%, 50%, and 80% of the channel length to calculate the angles. Thus, the angles are smaller than found in river networks, where $\beta_m = 72^\circ$ have been reported in the case of river networks in humid climates [21]. In such climates, rainfall can be expected to replenish the ground water across the system, unlike the case in our system where the fluid enters the domain from one of the boundaries. The systematic difference between the lower and higher domain aspect ratio also indicates that the branching angles depend on the geometry of the flow in the domain and are not universal in our system.

V. CONCLUSIONS

In conclusion, by performing experiments and simulations, we show that narrow channels develop in unconsolidated granular medium due to hydrodynamic forces exerted by the fluid flow moving through the medium. In the system studied, dissolution and cohesion are absent, and the fluid flow has to overcome only friction forces and local packing constraints in order to erode the medium. A curvature-driven feedback exists in these systems whereby erosion of the medium increases the conductivity in that region, thus drawing more fluid leading to a narrow channel which invades the medium [6]. Channels are observed to initiate at the outlet and develop headward toward the fluid source. Calculating the fluid flow in the medium, we demonstrate that spatial variations of the fluid flow can occur even with a narrow grain size dispersion and packing of the medium that has consequences for the development of internal erosion.

The conductivity variation within the medium can cause the channels not only to grow nonuniformly, but also bifurcate depending on the flow structure near the channel head. A single channel is observed to develop upstream if the flow is uniform. Branching is observed to occur when convergent flow develops near the channel head and when the flow is well above the threshold required to erode a channel. Under these conditions, the flow activates more than one site along the front causing it to erode in multiple directions. As these incipient channels occur, they draw fluid and thus erode faster at the expense of neighboring regions. This leads to coarsening whereby a single channel eventually dominates unless the bifurcation is driven by nonuniform source distribution.

While the branched channel network eroded by fluid flow may resemble a river network, their network characteristics show some similarities and differences. The number of branches are observed to grow sublinearly with the length of the channel, unlike river networks where the number of branches appear to grow exponentially [31]. This appears to be due to the fact that the fluid sources are located at the boundaries. Thus, side branches which grow earlier in the evolution are screened by the branches which grow later, closer toward the source. Hence, while new branches are created near the channel heads, the ones farther down are coarsened out as the main branches get wider or close off the branches with sediments. Further, the angles between neighboring branches are found to be distributed about a lower mean compared to river networks in humid climates, but more similar to those in arid climates [22]. The mean branching angles observed in our study vary with domain aspect ratio and thus do not appear to be universal.

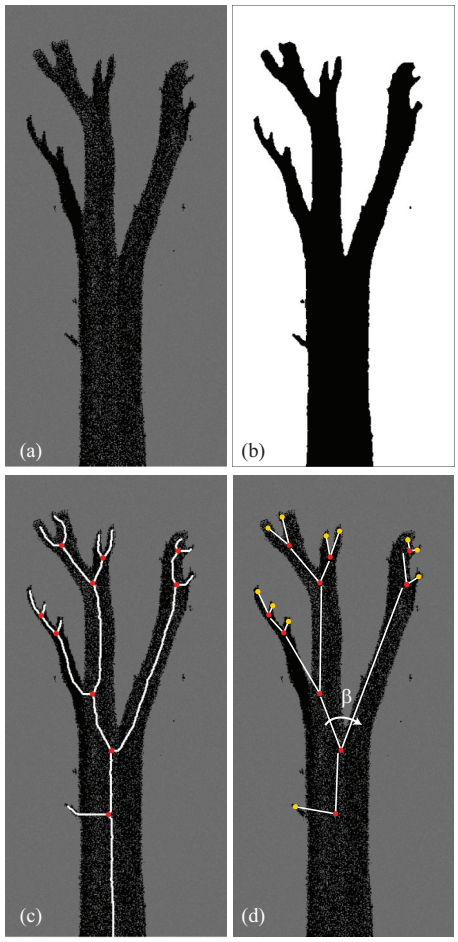

FIG. 13. (a) An example of an eroded channel observed in a simulation. (b) Corresponding filtered image where isolated eroded regions have been removed. (c) The skeleton of the channel network with bifurcation and channel heads identified. (d) Segments are used to join the branch points to the next branch points in the network or channel head. The angle between adjacent segments are use to identify branch angle β as shown.

ACKNOWLEDGMENTS

We thank B. Allen for discussions. This material is based upon work supported by the US Department of Energy Office of Science, Office of Basic Energy Sciences program under DE-FG02-13ER16401.

APPENDIX: IDENTIFICATION OF NETWORK CHARACTERISTICS

In order to analyze the growth of the channels, we use the Image Processing Toolbox in MATLAB to extract the main branches of the channel network, their heads, and bifurcation points. The main steps used in the image processing is outlined in Fig. 13. We first convert the raw image shown in Fig. 13(a) to a binary image as shown in Fig. 13(b). Then we reduce the binary image to a single-pixel-wide object by applying the morphological thinning function, which is an erosion-based process that removes the foreground pixels without breaking connected objects [32]. The branch points and end points of this object are then identified as shown in Fig. 13(c). We compute the angle between neighboring branches as shown in Fig. 13(d) by using the line segments joining the branch point to the next branch points in the hierarchy.

[1] A. Rinaldo, R. Rigon, J. R. Banavar, A. Maritan, and I. Rodriguez-Iturbe, Evolution and selection of river networks: Statics, dynamics, and complexity, Proc. Natl. Acad. Sci. USA **111**, 2417 (2014).

[2] P. Dietrich, *Flow and Transport in Fractured Porous Media* (Springer, New York, 2005).

[3] A. D. Howard and C. F. McLane, Erosion of cohesionless sediment by groundwater seepage, Water Resour. Res. **24**, 1659 (1988).

[4] P. S. Dodds and D. H. Rothman, Geometry of river networks. I. Scaling, fluctuations, and deviations, Phys. Rev. E **63**, 016115 (2000).

[5] T. Dunne, Formation and controls of channel networks, Prog. Phys. Geogr. **4**, 211 (1980).

[6] A. Kudrolli and X. Clotet, Evolution of Porosity and Channelization of an Erosive Medium Driven by Fluid Flow, Phys. Rev. Lett. **117**, 028001 (2016).

[7] A. D. Howard and C. G. Groves, Early development of karst systems. II. Turbulent flow, Water Resourc. Res. **31**, 19 (1995).

[8] J. Bautista and A. D. Taleghani, Dynamic modeling of injectivity evolution in unconsolidated sands, J. Petro. Sci. Eng. **149**, 256 (2017).

[9] P. Gouze and L. Luquot, X-ray microtomography characterization of porosity, permeability and reactive surface changes during dissolution, J. Contam. Hydrol. **120–121**, 45 (2011).

[10] P. Szymczak and A. J. C. Ladd, Instabilities in the dissolution of a porous matrix, Geophys. Res. Lett. **38**, L07403 (2011).

[11] G. Daccord and R. Lenormand, Fractal patterns from chemical dissolution, Nature (London) **325**, 41 (1987).

[12] O. Singurindy and B. Berkowitz, Evolution of hydraulic conductivity by precipitation and dissolution in carbonate rock, Water Resour. Res. **39**, 1016 (2003).

[13] O. Zvikelsky and N. Weisbrod, Impact of particle size on colloid transport in discrete fractures, Water Resour. Res. **42**, W12S08 (2006).

[14] H. M. D. Harshani, S. A. Galindo-Torres, A. Scheuermann, and H. B. Muhlhaus, Micro-mechanical analysis on the onset of erosion in granular materials, Philos. Mag. **95**, 3146 (2015).

[15] R. Jäger, M. Mendoza, and H. J. Herrmann, Channelization in porous media driven by erosion and deposition, Phys. Rev. E **95**, 013110 (2017).

[16] Ø. Johnsen, R. Toussaint, K. J. Måløy, and E. G. Flekkøy, Pattern formation during air injection into granular materials confined in a circular Hele-Shaw cell, Phys. Rev. E **74**, 011301 (2006).

[17] B. Sandnes, E. G. Flekkøy, H. A. Knudsen, K. J. Måløy, and H. See, Patterns and flow in frictional fluid dynamics, Nat. Commun. **2**, 288 (2011).

[18] R. L. Leheny and S. R. Nagel, Model for the Evolution of River Networks, Phys. Rev. Lett. **71**, 1470 (1993).

[19] J. T. Perron, P. W. Richardson, K. L. Ferrier, and M. Lapôtre, The root of branching river networks, Nature (London) **492**, 100 (2012).

[20] E. Shelef and G. E. Hilley, Symmetry, randomness, and process in the structure of branched channel networks, Geophys. Res. Lett. **41**, 3485 (2014).

[21] Y. Cohen, O. Devauchelle, H. F. Seybold, R. S. Yi, P. Szymczak, and D. H. Rothman, Path selection in the growth of rivers, Proc. Natl. Acad. Sci. USA **112**, 14132 (2016).

[22] H. Seybold, D. H. Rothman, and J. W. Kirchner, Climate's watermark in the geometry of stream networks, Geophys. Res. Lett. **44**, 2272 (2017).

[23] M. Berhanu, A. Petroff, O. Devauchelle, A. Kudrolli, and D. H. Rothman, Shape and dynamics of seepage erosion in a horizontal granular bed, Phys. Rev. E **86**, 041304 (2012).

[24] J. D. Pelletier and D. L. Turcotte, Shapes of river networks and leaves: Are they statistically similar? Phil. Trans. R. Soc. B **355**, 307 (2000).

[25] V. Fleury and J.-F. Gouyet, *Branching in Nature: Dynamics and Morphogenesis of Branching Structures, from Cell to River Networks* (Springer, New York, 2001).

[26] A. Mahadevan, A. V. Orpe, A. Kudrolli, and L. Mahadevan, Flow-induced channelization in a porous medium, Europhys Lett. **98**, 58003 (2012).

[27] A. E. Lobkovsky, B. Smith, A. Kudrolli, D. C. Mohrig, and D. H. Rothman, Erosive dynamics of channels incised by subsurface water flow, J. Geophys. Res. **112**, F03S12 (2007).

[28] A. Kudrolli, D. Scheff, and B. Allen, Critical shear rate and torque stability condition for a particle resting on a surface in a fluid flow, J. Fluid Mech. **808**, 397 (2016).

[29] A. Hong, M. Tao, and A. Kudrolli, Onset of erosion of a granular bed in a channel driven by fluid flow, Phys. Fluids **27**, 013301 (2015).

[30] R. J. Cornish, Flow in a pipe of rectangular cross-section, Proc. R. Soc. London A **120**, 691 (1928).

[31] E. V. Giusti and W. J. Schneider, The distribution of branches in river networks, Physiographic and hydraulic studies of rivers, Geological Survey Professional Paper 422-G (1965).

[32] L. Lam, S.-W. Lee, and C. Y. Suen, Thinning methodologies—A comprehensive survey, IEEE Trans. Pattern Anal. Machine Intel. **14**, 869 (1992).